Diffusion Flame of a CH$_4$/H$_2$ Jet in a Hot Coflow: Effects of Coflow Oxygen and Temperature[*]

MEI Zhenfeng (梅振锋), **WANG Feifei** (王飞飞) , **LI Pengfei** (李鹏飞) **and MI Jianchun** (米建春)[**]
State Key Laboratory of Turbulence & Complex Systems, Department of Energy & Resources Engineering, College of Engineering, Peking University, Beijing 100871, China

Abstract   This paper investigates the effects of coflow O$_2$ level and temperature on diffusion flame of a CH$_4$/H$_2$ jet in hot coflow (JHC) from a burner system similar to that of Dally *et al*. The coflow O$_2$ mass fraction ($y_{O_2}^*$) is varied from 3% to 80% and the temperature (T_{cof}^*) from 1200 K to 1700 K. The Eddy Dissipation Concept (EDC) model with detailed reaction mechanisms GRI-Mech 3.0 is used for all simulations. To validate the modeling, several JHC flames are predicted under the experimental conditions of Dally *et al*. [*Proc. Combust. Inst*., 29 (1), 1147−1154 (2002)] and the results obtained match well with the measurements. Results demonstrate that, when $y_{O_2}^*$ decreased, the diffusion combustion is likely to transform from traditional combustion to MILD (Moderate or Intense Low-oxygen Dilution) combustion mode. When T_{cof}^* is higher, the temperature distribution over the whole domain trends to be more uniform. Reducing $y_{O_2}^*$ or T_{cof}^* leads to less production of intermediate species OH and CO. It is worth noting that if $y_{O_2}^*$ is high enough ($y_{O_2}^*$ >80%), increasing $y_{O_2}^*$ does not cause obvious temperature increase.
Keywords   jet in hot coflow, moderate and intense low-oxygen dilution combustion, diffusion flame, intermediate specie

1   INTRODUCTION

Moderate or Intense Low-oxygen Dilution (MILD) combustion belongs to the volume combustion which is full of the furnace. Its general characteristics are low reaction rate, uniform thermal distribution, low combustion temperature, low noise and extremely low combustion-generated pollutants [1−5]. Compared to traditional combustion, it can improve thermal efficiency (thus reducing CO$_2$ emission) by more than 30% and reducing NO$_x$ emission by more than 70% [5]. This combustion, debuting in early 1990s, has been successfully utilized, particularly, in steel and metallurgy industries of many countries, *e.g.*, Germany, Italy, Japan, United States, Sweden and China. Due to its high thermal efficiency and low pollution emission, MILD combustion is considered as one of the most promising combustion technologies in the 21st century.

In the late two decades or so, MILD combustion has been increasingly studied. Szegö *et al*. [6] studied the effects of the inlet conditions (*i.e.* pre-heating temperature of the air, equivalence ratio, heat dissipation rate of the furnace, fuel dilution level) on establishing MILD combustion on a laboratory-scale furnace. They investigated the CO, NO$_x$ emission and stability characteristics of a parallel jet combustion system. Mi *et al*. [7, 8] performed experiments and computation on the same furnace to study the effects of the inlet momentum of the premixed jet of fuel and air on MILD combustion and emissions (*i.e.* CO, NO$_x$). They suggested that there was a critical momentum

rate of fuel-air mixture above which MILD combustion could be realized. Li *et al*. [9] studied the effect of pre-heating temperature of air on the characteristics of CH$_4$ combustion and NO emission by computation. They found that the NO emission concentration increased exponentially with pre-heating air temperature. Li *et al*. [10−12] and Mi *et al*. [13, 14] performed experiments and computations to study effects of inlet conditions of premixed and non-premixed jets on realizing MILD combustion. They reported that when the equivalence ratio was near 1, the combustion mode was still in the MILD mode and NO$_x$ emissions were low but extremely high CO and H$_2$ emissions were obtained. The studies [10−14] focused on the effects of inlet conditions but not on those of local quantities of the flue gases inside furnaces. This is not sufficient for the understanding of the mechanism of MILD combustion.

In the JHC open flame device used by Dally *et al*. [15], temperature and O$_2$ level of the surrounding hot coflow can be well controlled. Thus, the effects of thermal field and oxygen dilution of the recirculated hot flue gases in furnaces may be simulated by using the JHC device after removing the cold air coflow. Many simulations by computational fluid dynamics (CFD) of the MILD combustion [7−11, 16−19] have been performed. Christo *et al*. [16] and Mardani *et al*. [17] simulated the JHC experiment of Dally *et al* [15]. Comparison between the computation and the experiment showed that the Eddy Dissipation Concept (EDC) model [19] and detailed mechanisms by GRI-Mech 3.0 [20] could well predict the characteristics of flow and

flame in the MILD combustion. These well-proved models are used in the present study.

The present work is to first verify the RANS modeling by simulating the JHC combustion under the same condition of Dally et al [15]. Then, an investigation is carried out for the effects of the coflow O_2 level ($y_{O_2}^*$) and temperature (T_{cof}^*) on the JHC diffusion flame after removing the outer cold air. The objective is to clarify how $y_{O_2}^*$ and T_{cof}^* of the hot flue gas in furnaces impact the MILD combustion of gaseous fuel.

2 COMPUTATIONAL DETAILS

2.1 Configuration of the JHC burner of simulation

Figure 1 shows the structure of the JHC burner [15], from which the modeled flames are produced. It consists of an insulated and cooled central jet (inner diameter $D = 4.25$ mm) and an annulus nozzle (inner diameter = 82 mm) with an internal burner mounted upstream of the exit plane. The internal burner provides hot combustion products which are mixed with air and nitrogen via oxidant inlets to control the temperature

and O_2 levels in the mixture. The fuel is a mixture of H_2 and CH_4, equal in volume. In the experiment of Dally et al. [15], the JHC burner was mounted on a wind tunnel which provided a co-axial surrounding air stream at room temperature and with the same velocity as the hot coflow (3.2 m·s⁻¹). Their mass fraction of O_2 in the hot coflow ($y_{O_2}^*$) was operated at 3%, 6% and 9%.

To validate the RANS modeling, the flames from the above JHC burner are simulated under the identical conditions of Dally et al. [15], as Table 1 shows. However, to study the effects of coflow oxygen and temperature, the boundary conditions of the JHC burner [15] is modified by replacing the outer air stream with all hot coflow, as Fig. 2 (b) shows. The removal of the cold air is to ensure that $y_{O_2}^*$ and T_{cof}^* remain the same in the whole computational domain. This modification makes it possible to better investigate the effects of the coflow $y_{O_2}^*$, T_{cof}^* in the whole computational domain and mimic the effects of the local O_2 level and temperature of the hot recirculation flue gas inside furnaces with no interference by the outer cold air.
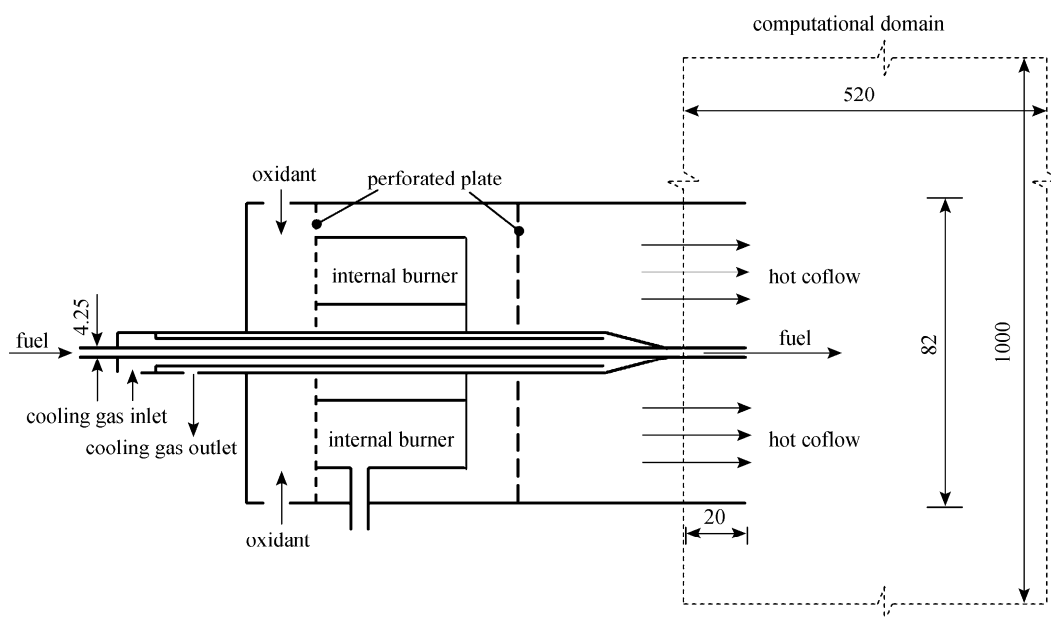

Figure 1   Structure of the JHC burner (in unit of mm)

Table 1   Inlet conditions of Dally et al.'s experiment [15] for firing CH_4/H_2

Fuel jet (CH_4/H_2)		Oxidant coflow (mass fraction)						Cold air (mass fraction)			
Re	T^*/K	T_{cof}^* /K	$y_{O_2}^*$ /%	$y_{N_2}^*$ /%	$y_{H_2O}^*$ /%	$y_{CO_2}^*$ /%	v_{cof}^* /m·s⁻¹	T_{air}^* /K	$y_{O_2,air}^*$ /%	$y_{N_2,air}^*$ /%	v_{air}^* /m·s⁻¹
9482	305	1300	3	85	6.5	5.5	3.2	300	23.3	76.7	3.2
9482	305	1300	6	82	6.5	5.5	3.2	300	23.3	76.7	3.2
9482	305	1300	9	79	6.5	5.5	3.2	300	23.3	76.7	3.2

(a) Experimental cases of Table 1 [12] (in unit of mm)

(b) Modified JHC burner for CFD cases of Table 2 (in unit of mm)
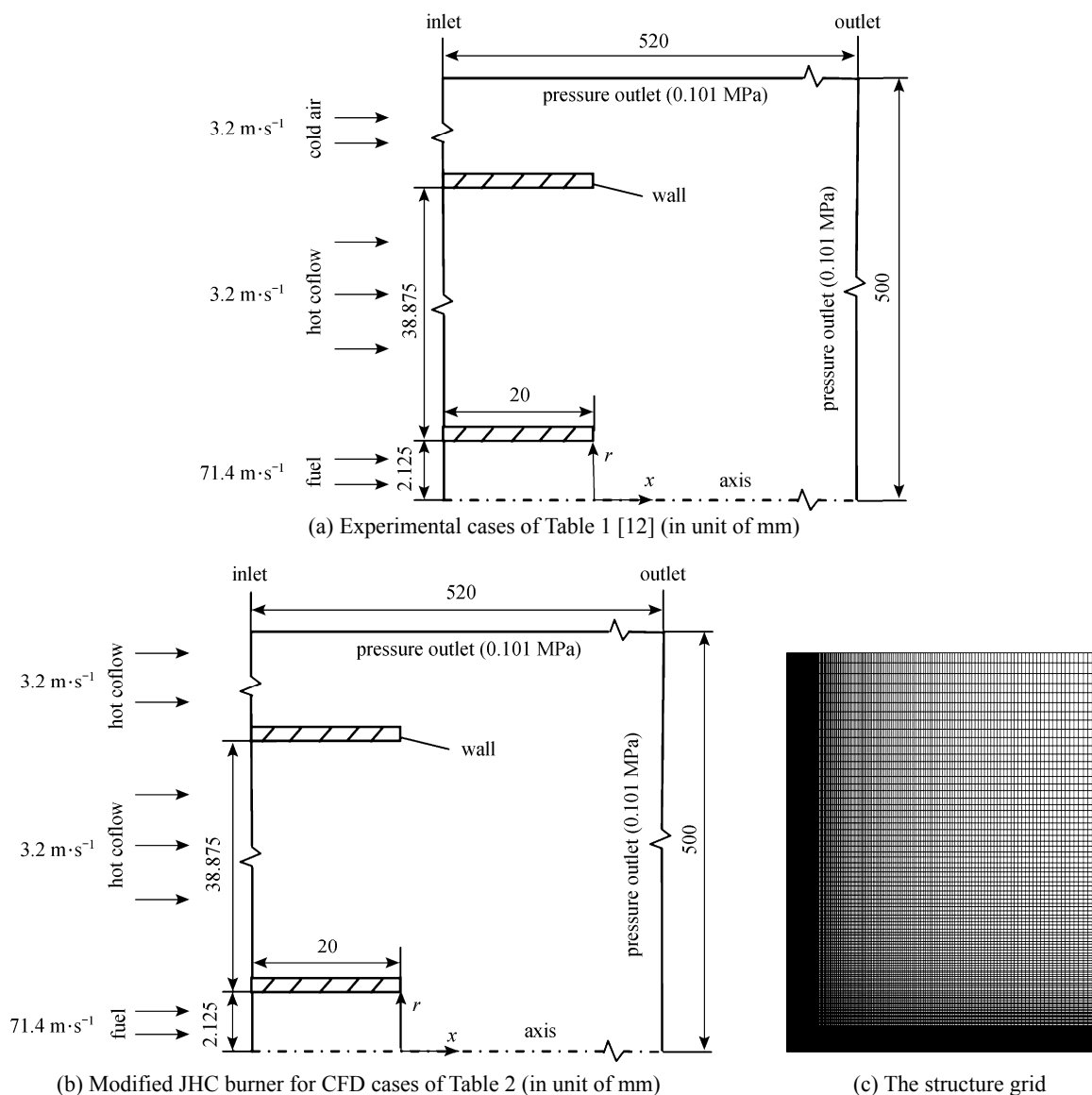

(c) The structure grid

Figure 2 Boundary conditions (a) experimental cases of Table 1 [15] for validation of numerical program, (b) modified JHC burner for CFD parametric study in Table 2, and (c) the structured grid

2.2 Computational models

Due to the symmetry of the system, a geometrically simplified axisymmetric computational model (2D) is constructed, as shown in Fig. 2. A primary orthogonal structured mesh with about 30000 cells in Fig. 2 (c) is used to simulate flames after verifying the grid-independency of the results using a finer grid with 130000 cells. The computational results for different grids are plotted by the dimensionless radial location r/D on the horizontal axis, the temperature (T) on the left vertical axis and OH mass fraction (y_{OH}) on the right vertical axis, see Fig. 3. Results (*i.e.* temperature, OH mass fractions) keep in high consistency for different grids, as Fig. 3 shows. The origin of the coordinate system is at the fuel nozzle exit (Fig. 2). The right

and upper boundary conditions are set to the pressure outlets, namely, the specification of a static (gauge) pressure enforced at the outlet boundary. The value of the specified static pressure is used only when the flow is subsonic. All other flow quantities are extrapolated from the flow in the interior.

In the present simulations, the standard k-ε model with the standard wall functions is used as the turbulent model. The standard k-ε model [21] is a semi-empirical model based on model transport equations for the turbulence kinetic energy (k) and its dissipation rate (ε):

$$\frac{\partial(\rho k)}{\partial t} + \frac{\partial(\rho k u_i)}{\partial x_i} = \frac{\partial}{\partial x_j}\left[\left(\mu + \frac{\mu_t}{\sigma_k}\right)\frac{\mathrm{d}k}{\mathrm{d}x_j}\right] + G_k + G_b - \rho\varepsilon - Y_M + S_k \qquad (1)$$

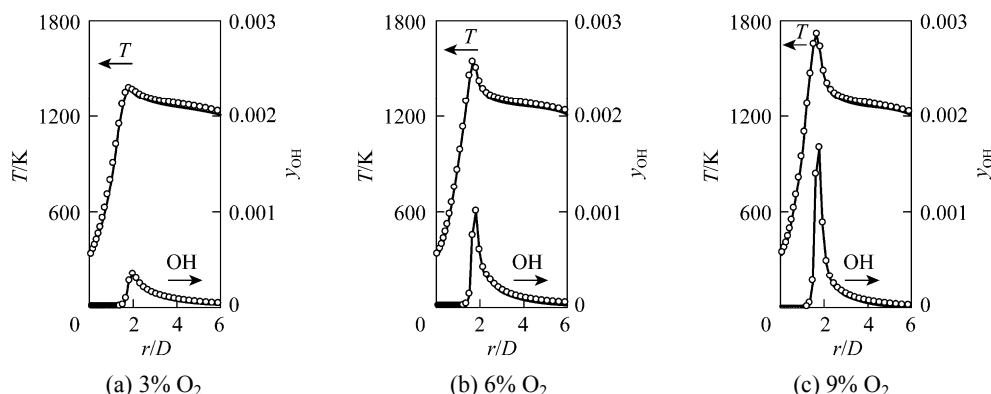(a) 3% O_2 (b) 6% O_2 (c) 9% O_2

Figure 3   **Temperature and OH mass fraction distribution at $x = 30$ mm for the two different grids** (curves for the gird with about 30000 cells, and symbols for the gird with about 130000 cells)

$$\frac{\partial(\rho\varepsilon)}{\partial t}+\frac{\partial(\rho\varepsilon u_i)}{\partial x_i}=\frac{\partial}{\partial x_j}\left[\left(\mu+\frac{\mu_t}{\sigma_k}\right)\frac{\partial\varepsilon}{\partial x_j}\right]+$$

$$C_{1\varepsilon}\frac{\varepsilon}{k}\left(G_k+C_{3\varepsilon}G_b\right)-C_{2\varepsilon}\rho\frac{\varepsilon^2}{k}+S_\varepsilon \qquad (2)$$

In these equations, ρ is the fluid density, x_i and x_j (i, $j = 1, 2, 3$) are the coordinates, u_i is the velocity components in three directions, μ is the dynamic viscosity, μ_t is the turbulent viscosity. G_k represents the generation of turbulence kinetic energy due to the mean velocity gradients whereas G_b is the generation of turbulence kinetic energy due to buoyancy. Y_M represents the contribution of the fluctuating dilatation in compressible turbulence to the overall dissipation rate. $C_{1\varepsilon}$, $C_{2\varepsilon}$ and $C_{3\varepsilon}$ are constants. σ_k and σ_ε are the turbulent Prandtl numbers for k and ε, respectively. S_k and S_ε are user-defined source terms. The μ_t is computed by combining k and ε as follows:

$$\mu_t=\rho C_\mu\frac{\varepsilon^2}{k} \qquad (3)$$

where C_μ is a constant. The model constants $C_{1\varepsilon}$, $C_{2\varepsilon}$, C_μ, σ_k and σ_ε are usually given as follows [21]: $C_{1\varepsilon} = 1.44$, $C_{2\varepsilon} = 1.92$, $C_\mu = 0.09$, $\sigma_k = 1.0$ and $\sigma_\varepsilon = 1.3$. As suggested in Ref. [16], the coefficient $C_{1\varepsilon}$ in the eddy dissipation equation should be varied from the standard value of 1.44 to the value of 1.6, which has been found to obtain the best agreements with experiments. The present study has therefore taken that $C_{1\varepsilon} = 1.6$. The discrete ordinate (DO) radiation model [18] with weighted sum of gray gas model (WSGGM) is employed as the radiation model.

The EDC model [19] with the detailed chemical kinetic mechanisms (GRI-Mech 3.0 [20]) is applied for the modeling of reactions. In the present study, the NO_x emission characteristics are not investigated. Thus the species and reactions involved with element N included in GRI-Mech 3.0 are eliminated. A modified GRI-Mech 3.0 which consists of 36 species and a total of 219 reversible reactions is applied. This has also been proved in Refs. [22, 23]. In EDC model, the species conservation equation for chemical species takes the following general form:

$$\frac{\partial(\rho Y_i)}{\partial t}+\nabla\cdot\left(\rho\boldsymbol{v}Y_i\right)=-\nabla\boldsymbol{J}_i+R_i \qquad (4)$$

where Y_i is the local mass fraction of each specie i, $\boldsymbol{v}$ is the velocity vector, $\boldsymbol{J}_i$ is the diffusion flux of specie i, and R_i is the net rate of production of species i by chemical reaction. The fine length scale (ξ) and the residence chemical time scale (τ) of fluid in the fine flow structures is expressed by

$$\xi=C_\xi\left(\frac{v\varepsilon}{k^2}\right), \quad \tau=C_\tau\left(\frac{v}{\varepsilon}\right)^{1/2} \qquad (5)$$

where C_ξ and C_τ are time scale constants equal to 2.138 and 0.408, respectively. R_i is computed for each mean species as

$$R_i=\frac{\rho\xi^2}{\tau(1-\xi^3)}\left(Y_i^*-Y_i\right) \qquad (6)$$

where Y_i^* is the fine-scale species mass fraction after reacting over τ. The evolution of Y_i^* depends also on the chemical kinetic mechanism. To reduce the computational cost of time integration, the in-situ adaptive tabulation (ISAT) model of Pope [24] is used. The accuracy is checked by lowering the ISAT error tolerance and ensuring results having no further change. The specific heat of species (C_p) is set to change with the temperature.

The SIMPLE algorithm method is utilized to solve the pressure-velocity coupling. The second-order upwind scheme is employed for discretizing the equations in order to improve the accuracy of the simulations. Convergence is obtained when (1) the residuals are less than 10^{-6} for the energy and 10^{-5} for all the other variables and (2) the variations of the downstream outlet temperature and velocity are allowed to be within 1 K (<0.1% of the outlet average temperature) and 0.001 m·s^{-1} (<0.1% of the outlet average velocity), respectively.

(a) Temprearure and OH mass fraction   (b) Mass fraction of O_2 and CO
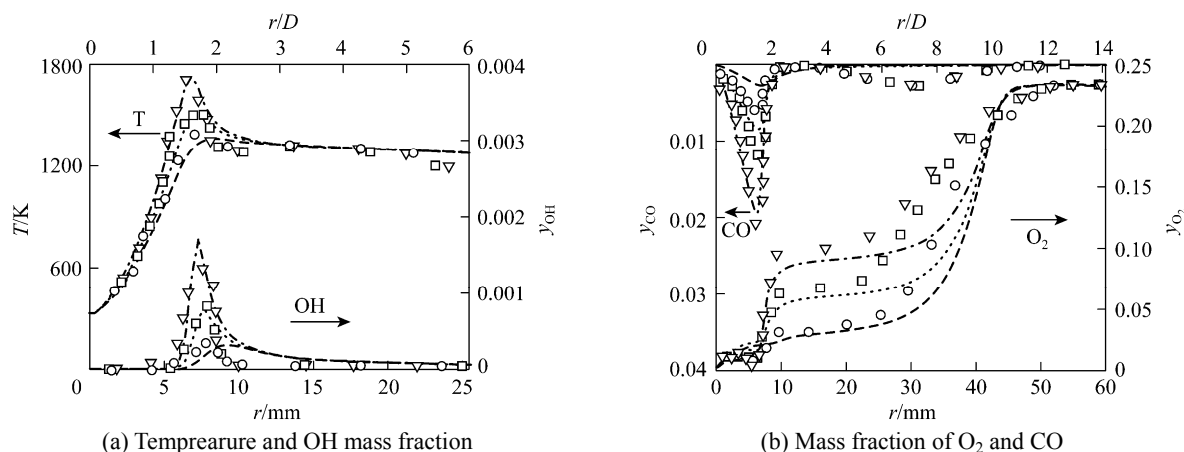
Figure 4   Comparison of numerical and exprimental profiles [15] of the temperatures (T) and other species mass fractions (y_{OH}, y_{O_2}, y_{CO}) at $x = 30$ mm

computation: ‑‑‑‑‑ $y^*_{O_2} = 9\%$; ······ 6%; ‑ ‑ ‑ 3%; experiment: ▽ 9%; □ 6%; ○ 3%

3   RESULTS AND DISCUSSION

3.1   Comparison between the present computation and previous experiment [15]

To verify the numerical predictions, comparison is made between the numerical results and the experimental data [15]. Fig. 4 compares the numerical and exprimental profiles of the temperatures (T) and species mass fractions (y_{OH}, y_{O_2}, y_{CO}) obtained at $x = 30$ mm. It is shown that the radial profiles of the temperature and OH mass fraction are predicted quite satisfactorily. The difference of the temperature peak between the computation and the experiment is smaller than 1.5% (about 20 K). Fig. 4 (b) demonstrates that the variation trends of the CO and O_2 mass fractions agree reasonably well with the experimental data. Fig. 5 compares the present predictions (curves) and the previous measurements (dots) [15] of the mixture fraction (ξ) obtained from Bilger's formula [25] for $y^*_{O_2} = 3\%$, along the jet axis and the radial direction at $x = 30$ mm, 60 mm and 120 mm. Obviously, the predictions agree quite well with the measurements. This suggests that the RANS modeling used presently can approximately capture the features of the diffusion combustion process.

3.2   Effects of outer cold air on the flame structure

Figure 6 shows the flames of Dally *et al.* [15] for $y^*_{O_2} = 3\%$, 6% and 9%. Evidently, when $y^*_{O_2} = 3\%$, there is no luminous flame in the region near the exit of the fuel jet; namely, it is in the MILD combustion mode over there. However, at about 100 mm above the jet exit, the outer cold air is entrained into the hot
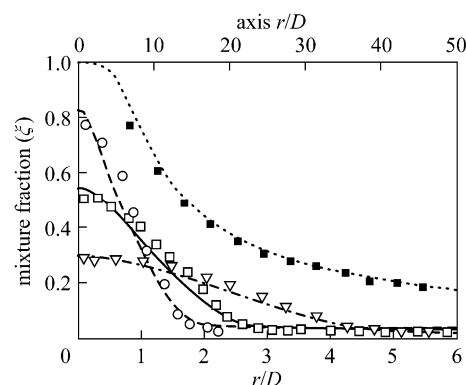

Figure 5   Comparison of the present predictions (curves) and the previous experiments (dots) [15] of the mixture fraction for $y^*_{O_2} = 3\%$

computation: ······ along the centreline; ‑ ‑ ‑ $x = 30$ mm; —— $x = 60$ mm; ‑‑‑‑‑ $x = 120$ mm; experiment: ■ along the centreline; ○ $x = 30$ mm; □ $x = 60$ mm; ▽ $x = 120$ mm

coflow and starts to influence the flame, consequently making it luminous due to higher oxidation rates. In the experiment, only the data in the region near the exit of fuel jet (*i.e.* $x \leqslant 30$ mm) may be appropriately used to investigate effects of $y^*_{O_2}$ or T^*_{cof} on the MILD diffusion combustion.

Temperature contours of the JHC flame for the case of Dally *et al.* [15] and that without an outer cold air coflow are shown in Figs. 7 (a) and 7 (b), respectively. As expected, the temperature distributions for the two cases are very different in the downstream region at $x > 30$ mm. In the case with an outer cold air coflow, similar to the experiment, the temperature in the mixing layer seems to be much higher than T^*_{cof} downstream from $x = 100$ mm, due to more oxygen entrained into the hot coflow. By comparison, see Fig. 7 (b), the
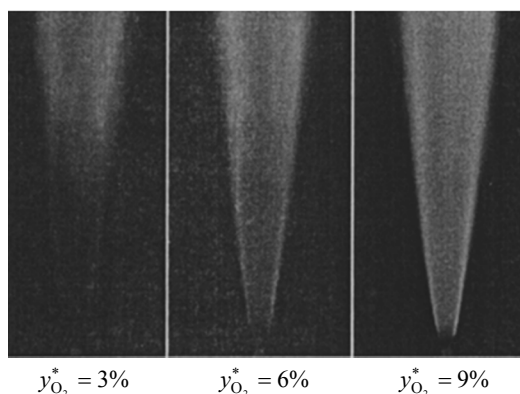
$y_{O_2}^* = 3\%$ $y_{O_2}^* = 6\%$ $y_{O_2}^* = 9\%$

Figure 6   **Photographs of flames reproduced from Dally** *et al.* **[15]**

temperature is only slightly higher than T_{cof}^* in the mixing layer of the jet with no cold air coflow. Obviously the outer cold air has a significant impact on the downstream combustion process. Thus, the following study is focused on the cases without air outside, to investigate the effects of $y_{O_2}^*$ and T_{cof}^*.

3.3   Effects of coflow O₂ level ($y_{O_2}^*$) on the flame structure

As listed in Table 2, $y_{O_2}^*$ is varied from 80% to 3% with T_{cof}^* kept at 1300 K. Fig. 8 shows that as $y_{O_2}^*$ decreases, the peak temperature, OH and H₂CO mass fractions decrease. The temperature and OH fields
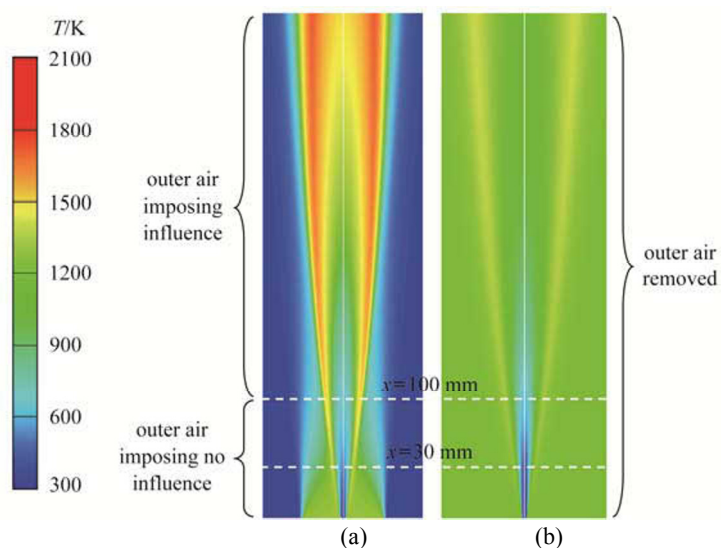
Figure 7   **Temperature contours of the JHC flame at** $y_{O_2}^* = 3\%$ [(a) with an outer cold air coflow; (b) without an outer cold air coflow]

Table 2   **Specifications of numerical conditions for the present research**

	Case	Fuel jet (CH₄/H₂)		Oxidant coflow (mass fraction)				
		Re	T^* /K	T_{cof}^* /K	$y_{O_2}^*$/%	$y_{N_2}^*$/%	$y_{H_2O}^*$/%	$y_{CO_2}^*$/%
varying $y_{O_2}^*$	1	9482	305	1300	80	8	6.5	5.5
	2	9482	305	1300	60	28	6.5	5.5
	3	9482	305	1300	40	48	6.5	5.5
	4	9482	305	1300	23.3	64.7	6.5	5.5
	5	9482	305	1300	12	76	6.5	5.5
	6	9482	305	1300	6	82	6.5	5.5
	7	9482	305	1300	3	85	6.5	5.5
varying T_{cof}^*	8	9482	305	1700	6	82	6.5	5.5
	9	9482	305	1600	6	82	6.5	5.5
	10	9482	305	1500	6	82	6.5	5.5
	11	9482	305	1400	6	82	6.5	5.5
	12	9482	305	1300	6	82	6.5	5.5
	13	9482	305	1200	6	82	6.5	5.5

(a) Temperature field   (b) OH distribution   (c) H$_2$CO distribution
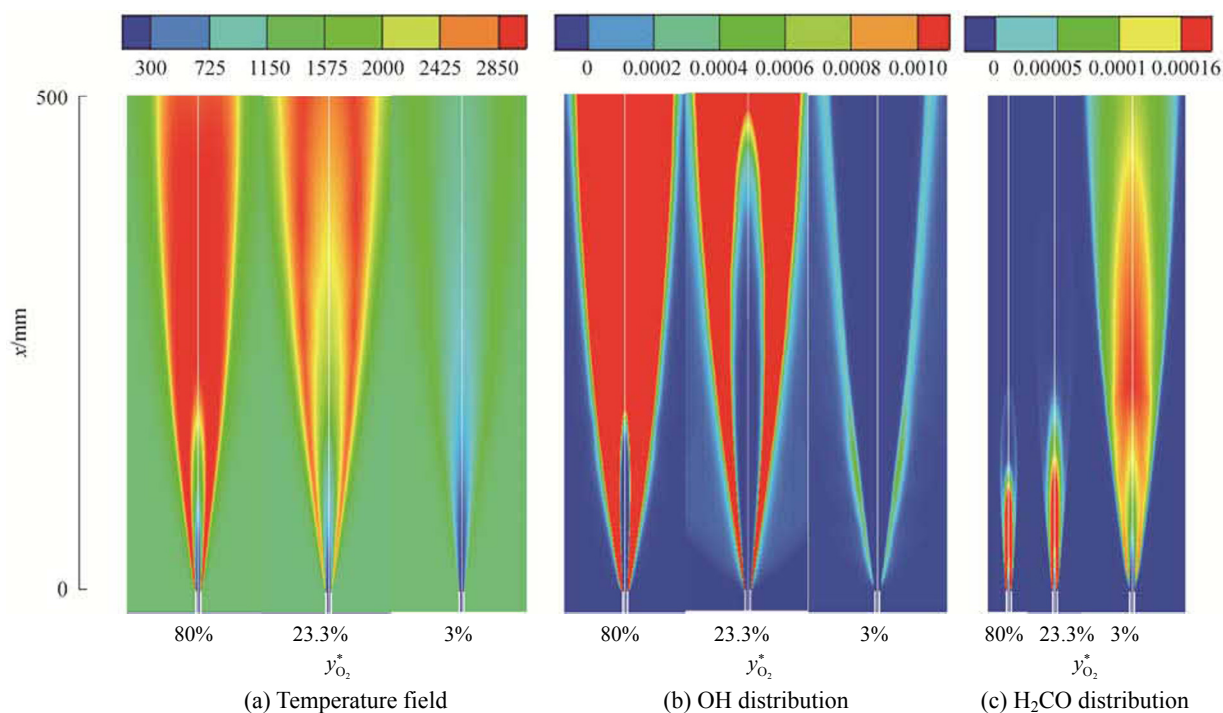
Figure 8   Temperature field, OH distribution and H$_2$CO distribution in the whole computational domain with different $y_{O_2}^*$

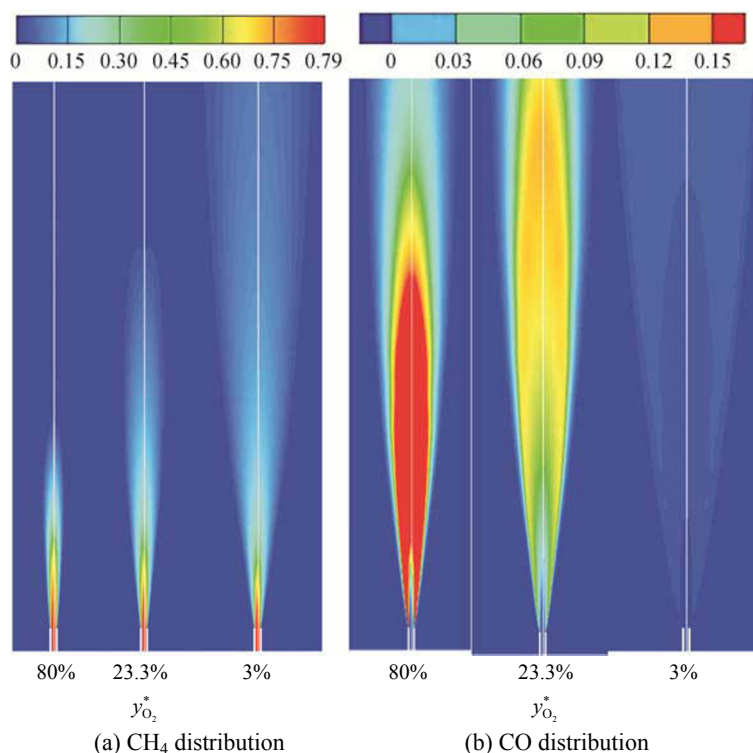(a) CH$_4$ distribution   (b) CO distribution

Figure 9   CH$_4$ distribution and CO distribution in the whole computational domain with different $y_{O_2}^*$

become more uniform. OH exists primarily in the high-temperature area while H$_2$CO is mainly in the low-temperature region. H$_2$CO is an intermediate species in the oxidation of most hydrocarbon fuels. It is found

typically in MILD combustion regime [26]. There is an area near the fuel jet exit where the H$_2$CO mass fraction is 0. It means no reaction occurs in that area. Fig. 9 shows that, as $y_{O_2}^*$ decreases, CH$_4$ and CO mass
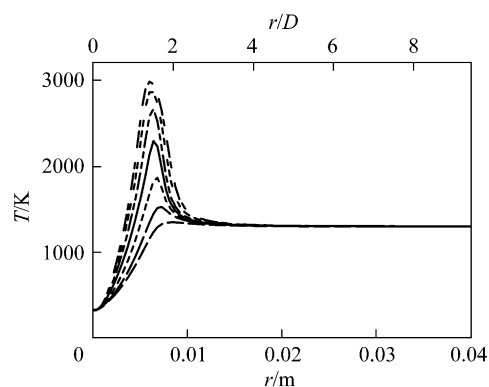
(a) $x = 30$ mm
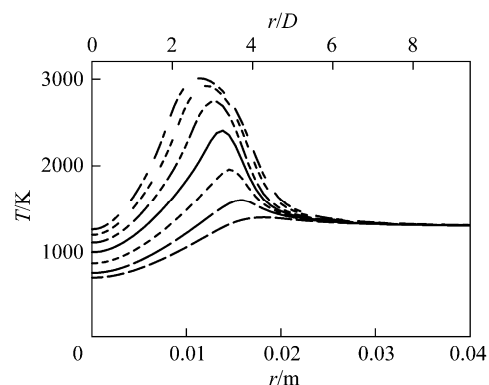
(b) $x = 100$ mm
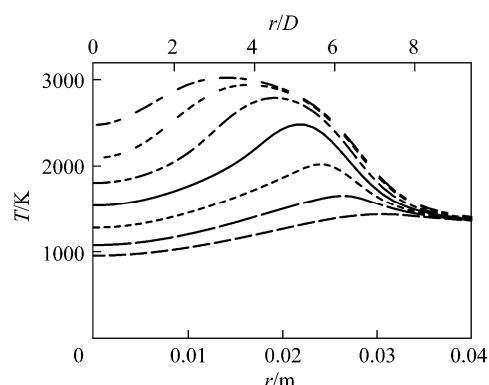
(c) $x = 200$ mm

Figure 10   Radial profiles of mean temperature for Cases 1−7

$\cdots\cdots y^*_{O_2} = 80\%$; $---\ --- y^*_{O_2} = 60\%$; $\cdots\cdots y^*_{O_2} = 40\%$;
$\text{——} \ y^*_{O_2} = 23.3\%$; $------ y^*_{O_2} = 12\%$; $\text{—— ——} y^*_{O_2} = 6\%$;
$\text{——} \ y^*_{O_2} = 3\%$
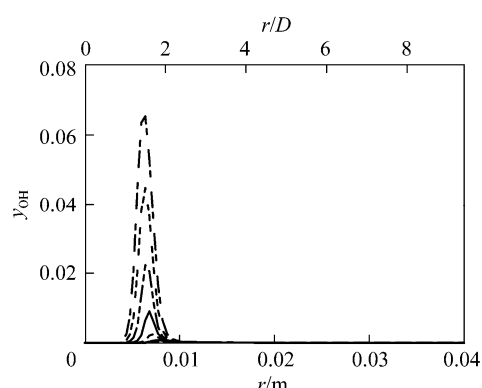
(a) $x = 30$ mm
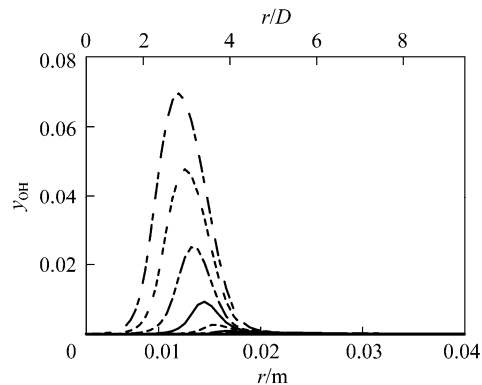
(b) $x = 100$ mm
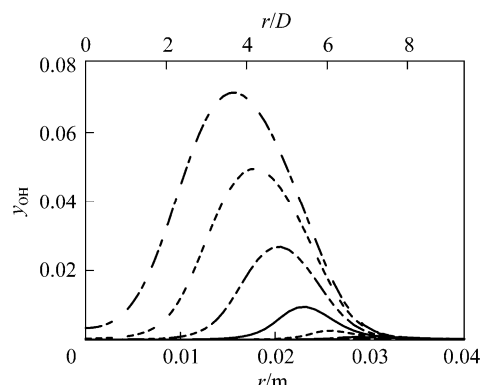
(c) $x = 200$ mm

Figure 11   Radial profiles of mean mass fraction of OH for Cases 1−7

$\cdots\cdots y^*_{O_2} = 80\%$; $---\ --- y^*_{O_2} = 60\%$; $\cdots\cdots y^*_{O_2} = 40\%$;
$\text{——} \ y^*_{O_2} = 23.3\%$; $------ y^*_{O_2} = 12\%$; $\text{—— ——} y^*_{O_2} = 6\%$;
$\text{——} \ y^*_{O_2} = 3\%$

fraction decrease. That is, decreasing $y^*_{O_2}$ generally leads to less consumption of CH_4, thus less production of CO. In addition, it takes a longer distance to burn out CH_4 and CO when $y^*_{O_2}$ decreases.

Additionally, Dally *et al*. [15] showed that, in the case with $y^*_{O_2} = 3\%$, at $x = 30$ mm, the temperature rise is about 100 K, OH mass fraction peak is about 3.5×10^{-4} and no luminous flame can be seen in their photographs. Namely, the combustion is in the MILD

mode. When $y^*_{O_2}$ increases to 9%, they found that at $x = 30$ mm, the peak temperature is about 400 K higher than the T^*_{cof} and OH mass fraction peak is about 13.2×10^{-4}, thus traditional luminous flame occurs. Thus, in the present study, the experimental data is used to judge the MILD combustion obtained when (1) the temperature rise is smaller than 300 K and (2) OH mass fraction peak is smaller than 6×10^{-4}. As Figs. 10−12 show, it can be easily inferred that Case 7 is in

the MILD mode while Cases 1−6 in traditional mode. Moreover, in the MILD mode in Case 7, the maximums of CH_3, H_2CO and CO (the unburnt species) mass fraction are 1.1×10^{-4}, 1.5×10^{-4} and 4.13×10^{-3}, respectively. As $y_{O_2}^*$ decreases, classical flame mode tends to be transformed to MILD one.

As demonstrated in Fig. 12, the temperature rise ($\Delta T_{max} = T_{max} - T_{cof}^*$) over the whole computational domain increases with $y_{O_2}^*$ and when $y_{O_2}^*$ is high enough ($y_{O_2}^* > 80\%$), the temperature rises to a constant. Namely, increasing $y_{O_2}^*$ cannot improve the temperature rise infinitely.
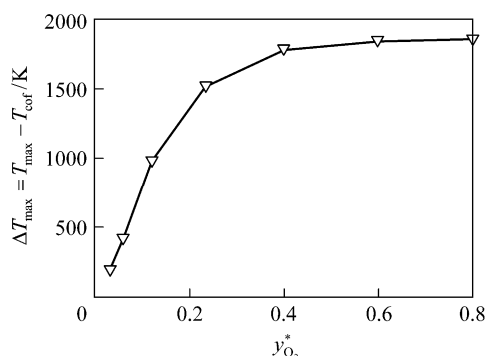
Figure 12 Effects of $y_{O_2}^*$ on the temperature rise ($\Delta T_{max} = T_{max} - T_{cof}^*$) over the whole computational domain

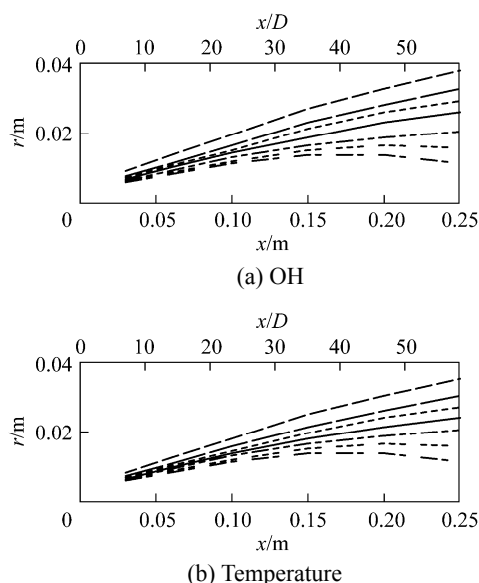Figure 13 shows the radial location of the maximum temperature ($r_{T_{max}}$) and OH mass fraction ($r_{OH_{max}}$)

(a) OH

(b) Temperature

Figure 13 Radial location of the maximum temperature and the maximum OH mass fraction for Cases 1−7
$----\ y_{O_2}^* = 80\%$; $---\ ---\ y_{O_2}^* = 60\%$; $------\ y_{O_2}^* = 40\%$; ——— $y_{O_2}^* = 23.3\%$; $------\ y_{O_2}^* = 12\%$; ——— $y_{O_2}^* = 6\%$; $---\ ---\ y_{O_2}^* = 3\%$

for Cases 1−7. OH is a vital intermediate and extremely useful in diagnostics usually as flame marker [27]. As demonstrated, decreasing $y_{O_2}^*$ causes $r_{T_{max}}$ and $r_{OH_{max}}$ increase. Worth noting that $r_{OH_{max}}$ is always a little larger than $r_{T_{max}}$ (about 2 mm). This could be well explained. The magnitude of OH mass fraction is mainly governed by two elementary reactions as follows [28]:

$$H + O_2 \longrightarrow OH + O \qquad (7)$$

$$CO + OH \longrightarrow CO_2 + H \qquad (8)$$
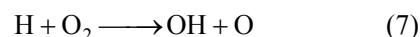
Due to the relatively high activation energy of reaction (7) (about 60.3 kJ·mol^{-1}), OH occurs primarily in relatively high temperature region. In the conditions of 298.15 K and 101.32 kPa, its reaction heat is about +70.5 kJ·mol^{-1} (endothermic reaction) and the reaction heat of reaction (8) is about −104.3 kJ·mol^{-1} (exothermic reaction). At the position of the maximum OH mass fraction in the mean reaction zone, much OH is produced by reaction (7). Then, OH is consumed in the downstream and releases much heat due to the following reaction (8). Thus, $r_{OH_{max}}$ always peaks slightly farther than $r_{T_{max}}$.

3.4   Effects of the hot coflow temperature (T_{cof}^*) on the flame structure

Figures 14 and 15 show that as T_{cof}^* decreases, the peaks of the temperature, OH and CO mass fractions decrease while the peak of the H_2CO mass fraction increases. That is, decreasing T_{cof}^* generally leads to less consumption of CH_4, thus produces less OH and CO. Here the effect of T_{cof}^* on H_2CO is contrary to $y_{O_2}^*$. This is because when temperature is high, H_2CO is consumed rapidly and resides quite shorter, so cannot be measured.

Figures 16 and 17 show that Cases 8−12 should be in classical mode. For Case 13 with $T_{cof}^* = 1200$ K, at $x = 30$ mm, the temperature peak is only slightly above T_{cof}^* (about 70 K) and a very small amount of OH radicals (about 2.5×10^{-4}) is produced due to combustion; but at $x = 200$ mm, the temperature rise is about 400 K and OH mass fraction is about 6.0×10^{-4}. Thus, Case 13 should be in classical mode.

Figure 18 shows the effects of T_{cof}^* on the temperature rise ($\Delta T_{max} = T_{max} - T_{cof}^*$) over the whole computational domain. It is know that specific heats of flue gases such as CO_2, N_2, O_2 and H_2O all increase with T_{cof}^*, so that the same amount of heat releasing from combustion causes the temperature to rise less when the coflow temperature is higher. At the same
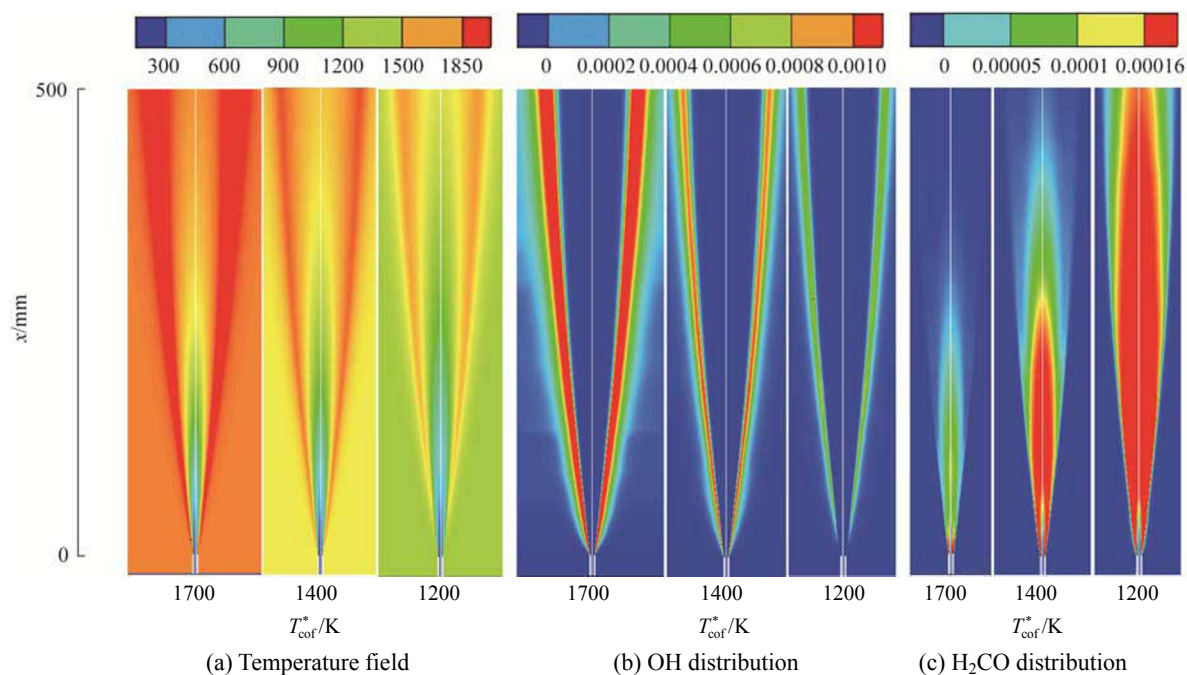
(a) Temperature field   (b) OH distribution   (c) H₂CO distribution

Figure 14   Temperature field, OH distribution and H$_2$CO distribution in the whole computational domain with different T_{cof}^*

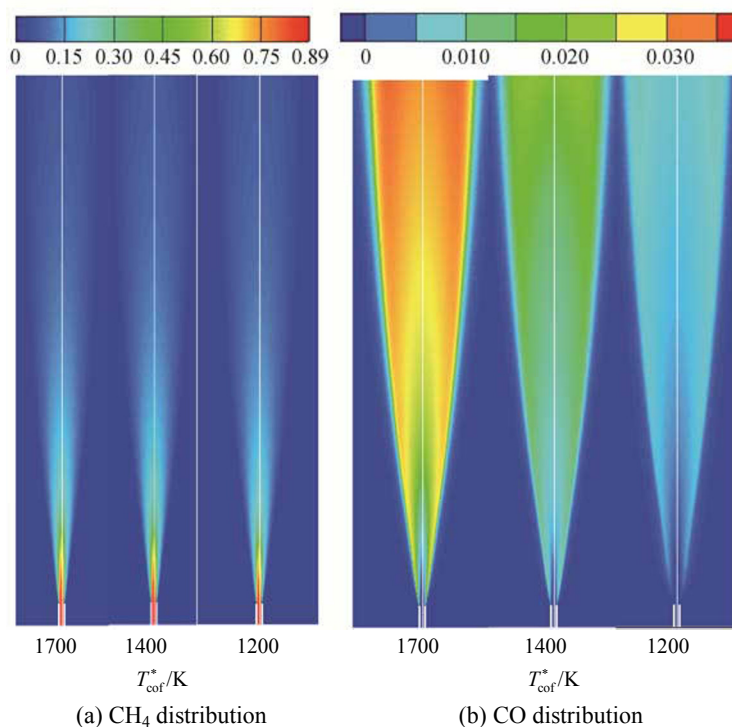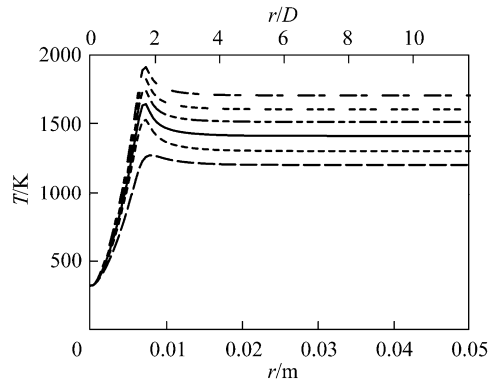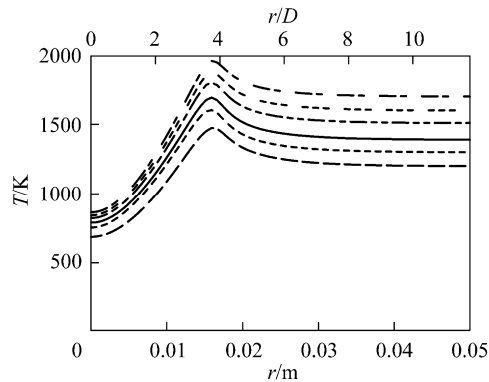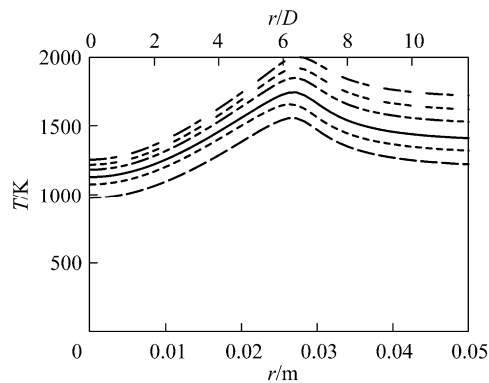(a) CH$_4$ distribution   (b) CO distribution

Figure 15   CH$_4$ distribution and CO distribution in the whole computational domain with different T_{cof}^*

time, the combustion reaction rate increases as T_{cof}^* increases. Whether the temperature rise (ΔT_{max}) over the whole domain increases or decreases depends on which effect is more significant. As shown in Fig. 18, when T_{cof}^* is higher, ΔT_{max} over the whole domain tends to be smaller; in other words, the temperature distribution tends to be more uniform. Nevertheless, Fig. 18 indicates that in industrial applications, the higher the coflow air is preheated, the more uniform the temperature distribution is achieved.

Figure 19 shows that as T_{cof}^* decreases, $r_{OH_{max}}$ and $r_{T_{max}}$ are almost to be the same. Varying T_{cof}^* has
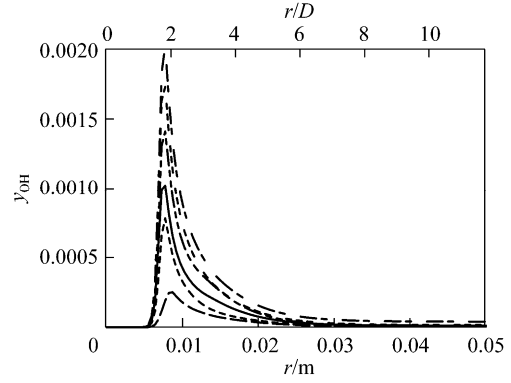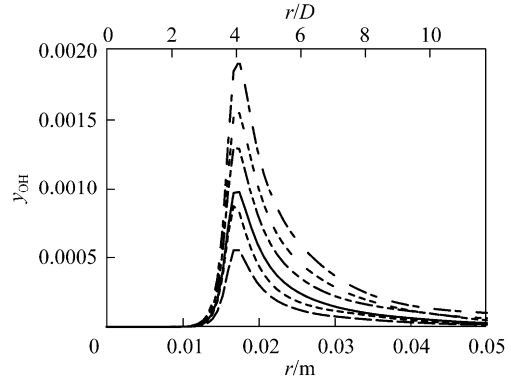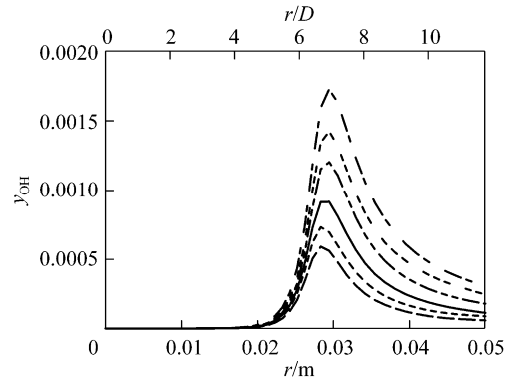
(a) $x = 30$ mm

(b) $x = 100$ mm

(c) $x = 200$ mm

Figure 16   Radial distributions of the mean temperature (T) for Cases 8−13

------ $T_{cof}^* = 1700$ K; --- --- $T_{cof}^* = 1600$ K;
-----·· $T_{cof}^* = 1500$ K; —— $T_{cof}^* = 1400$ K;
------ $T_{cof}^* = 1300$ K; ——— $T_{cof}^* = 1200$ K

(a) $x = 30$ mm

(b) $x = 100$ mm

(c) $x = 200$ mm

Figure 17   Radial distributions of the mean OH concentration (y_{OH}) for Cases 8−13

------ $T_{cof}^* = 1700$ K; --- --- $T_{cof}^* = 1600$ K;
-----·· $T_{cof}^* = 1500$ K; —— $T_{cof}^* = 1400$ K;
------ $T_{cof}^* = 1300$ K; ——— $T_{cof}^* = 1200$ K

little effect on $r_{OH_{max}}$ and $r_{T_{max}}$. Similar to Fig. 13, Fig. 19 also shows that $r_{OH_{max}}$ is slightly larger than $r_{T_{max}}$.

4   CONCLUSIONS

The present study has numerically investigated the effects of the coflow O_2 level ($y_{O_2}^*$) and temperature (T_{cof}^*) on non-premixed MILD combustion produced

by a JHC burner [15] fed with the CH_4/H_2 mixture. The EDC model with detailed chemical mechanism (modified GRI-Mech 3.0) is implemented for the simulation. The computational results are in good agreement with the experimental data [15]. Based on the analysis on the computational results, several conclusions can be drawn below:

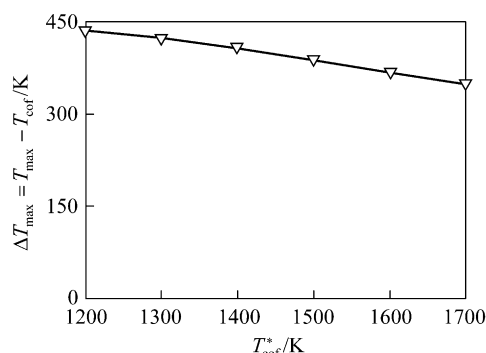(1) As $y_{O_2}^*$ decreases, the radial profiles of temperature distribution is more uniform, the combustion

Figure 18   Effects of T_{cof}^* on the temperature rise ($\Delta T_{\text{max}} = T_{\text{max}} - T_{\text{cof}}^*$) over the whole computational domain

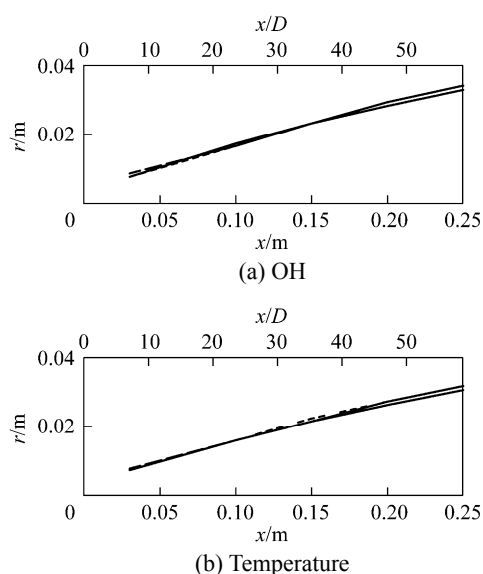
(a) OH

(b) Temperature

Figure 19   Radial location of the maximum temperature and the OH mass fraction for Cases 8−13
----- $T_{\text{cof}}^* = 1700$ K;   --- --- $T_{\text{cof}}^* = 1600$ K;
------ $T_{\text{cof}}^* = 1500$ K;   ——— $T_{\text{cof}}^* = 1400$ K;
------ $T_{\text{cof}}^* = 1300$ K;   — — $T_{\text{cof}}^* = 1200$ K

mode can be transformed from classical combustion mode to MILD mode; the peaks of temperature, intermediate specie OH, H_2CO and CO mass fraction in the computational region are severely suppressed. It takes a longer distance to burn out CH_4 and CO when $y_{O_2}^*$ decreases. If $y_{O_2}^*$ is high enough ($y_{O_2}^* > 80\%$), increasing $y_{O_2}^*$ leads to little combustion temperature increase.

(2) As T_{cof}^* decreases, the peaks of temperature and OH mass fraction decrease while H_2CO mass fraction peak increases. When T_{cof}^* is higher, the temperature distribution over the whole domain trends to be more uniform. It suggests that in industrial applications, the higher the combustion air is preheated, the more uniform the temperature distribution is achieved.

(3) Reducing $y_{O_2}^*$ causes the radial locations of the maximum OH mass fraction and the maximum temperature further away from the axis, while varying T_{cof}^* affects them quite slightly. It is interesting that the radial location of the maximum OH mass fraction is always slightly farther away from the axis than that of the maximum temperature.

NOMENCLATURE

k	turbulence kinetic energy, $m^2 \cdot s^{-2}$
$r_{\text{OH}_{\text{max}}}$	radial location of the maximum OH mass fraction, mm
$r_{T_{\text{max}}}$	radial location of the maximum temperature, mm
T_{cof}^*	coflow temperature, K
T	temperature, K
T_{max}	maximum temperature in the whole computational domain, K
ΔT_{max}	temperature rise $\Delta T_{\text{max}} = T_{\text{max}} - T_{\text{cof}}^*$, K
x	axial distance from the fuel exit
y_{OH}	OH mass fraction
y_{O_2}	O_2 mass fraction
y_{CO}	CO mass fraction
$y_{O_2}^*$	coflow oxygen mass fraction
ε	dissipation rate of turbulence kinetic energy, $m^2 \cdot s^{-2}$

REFERENCES

1   Li, P., Mi, J., Dally, B.B., Wang, F., Wang, L., Liu, Z., Chen, S., Zheng, C., "Progress and recent trend in MILD Combustion", *Sci. China Tech. Sci.*, **54** (2), 255−269 (2011).

2   Katsuki, M., Hasegawa, T., "The science and technology of combustion in highly preheated air", *Proc. Combust. Inst.*, **27** (2), 3135−3146 (1998).

3   Cavaliere, A., De, Joannon, M., "Mild combustion", *Prog. Energ. Combust.*, **30** (4), 329−366 (2004).

4   De Joannon, M., Langella, G., Beretta, F., Cavliere, A., Noviello, C., "Mild combustion: Process features and technological constrains", *Combust. Sci. Technol.*, **153** (1), 33−50 (2000).

5   Tsuji, H., Gupta, A., Hasegawa, T., Katsuki, M., Kishimoto, K., Morita, M., High Temperature Air Combustion: From Energy Conservation to Pollution Reduction, CRC Press, Florida (2003).

6   Szegö, G.G., Dally, B.B., Nathan, G.J., "Operational characteristics of a parallel jet MILD combustion burner system", *Combust. Flame*, **156** (2), 429−438 (2009).

7   Mi, J., Li, P., Dally, B.B., Craig, R.A., Wang, F., "Importance of initial momentum rate and air-fuel premixing on moderate or intense low oxygen dilution (MILD) combustion in a recuperative furnace", *Energy Fuels*, **23** (11), 5349−5356 (2009).

8   Mi, J., Li, P., Zheng, C., "Numerical simulations of flameless premixed combustion in a recuperative furnace", *Chin. J. Chem. Eng.*, **18** (1), 10−17 (2010).

9   Li, Y., Qi, H., Yuan, J., "Numerical Analysis of high temperature combustion of methane", *Journal of Engineering Thermophysics*, **22** (2), 257−260 (2001). (in Chinese)

10   Li, P., Mi, J., Dally, B.B., Craig, R.A., Wang, F., "Premixed moderate or intense low-oxygen dilution (MILD) combustion from a single jet burner in a laboratory-scale furnace", *Energy Fuels*, **25** (7), 2782−2793 (2011).

11   Li, P., Mi, J., Wang, F., "Effect of equivalence ratio and reactants mixing pattern on flameless combustion", *Proc. CSEE*, **31** (5), 20−27 (2011). (in Chinese)

12 Li, P., Dally, B.B., Mi, J., Wang, F., "MILD oxy-combustion of gaseous fuels in a laboratory-scale furnace", *Combust. Flame*, **160** (5), 933−946 (2013).

13 Mi, J., Li, P., Zheng, C., "Impact of injection conditions on flame characteristics from a parallel multi-jet burner", *Energy*, **36** (11), 6583−6595 (2011).

14 Mi, J., Wang, F., Li, P., Dally, B.B., "Modified vitiation by operational parameters in a MILD combustion furnace", *Energy Fuels*, **26** (1), 265−277 (2012).

15 Dally, B.B., Karpetis, A.N., Barlow, R.S., "Structure of turbulent non-premixed jet flames in a diluted hot coflow", *Proc. Combust. Inst.*, **29** (1), 1147−1154 (2002).

16 Christo, F.C., Dally, B.B., "Modeling turbulent reacting jets issuing into a hot and diluted coflow", *Combust. Flame*, **142**, 117−129 (2005).

17 Mardani, A., Tabejamaat, S., Ghamari, M., "Numerical study of influence of molecular diffusion in the MILD combustion regime", *Combust. Theor. Model.*, **14**, 747−774 (2010).

18 Chui, E.H., Raithby, G.D., "Computation of radiant heat transfer on a nonorthogonal mesh using the finite-volume method", *Numer. Heat Transfer B Fund.*, **23**, 269−288 (1993).

19 Magnussen, B.F., Hjertager, B.H., "On mathematical modeling of turbulent combustion with special emphasis on soot formation and combustion", *Symp. (Int.) Combust.*, **16** (1), 719−729 (1977).

20 Smith, G.P., Golden, D.M., Frenklach, M., Moriarty, N.W., Eiteneer, B., Goldenberg, M., Bownan, C.T., Hanson, R.K., Song, S., Gardiner, W.C, Lissianski, Jr.V.V., Qin, Z., "GRI-Mech 3.0", http://www.me.berkeley.edu/gri_mech/.

21 Lauder, B.E., Spalding, D.B., Lectures in Mathematical Models of Turbulence, Academic Press, London (1972).

22 Galletti, C., Parente, A., Derudi, M., Rota, R., Tognotti, G., "Numerical and experimental analysis of NO emissions from a lab-scale burner fed with hydrogen-enriched fuels and operating in MILD combustion", *Int. J. Hydrogen Energy*, **34** (19), 8339−8351 (2009).

23 Parente, A., Galletti, C., Tognotti, L., "Effect of the combustion model and kinetic mechanism on the MILD combustion in an industrial burner fed with hydrogen enriched fuels", *Intl. J. Hydrogen Energy*, **33** (24), 7553−7564 (2008).

24 Pope, S.B., "Computationally efficient implementation of combustion chemistry using in situ adaptive tabulation", *Combust. Theor. Model*, **1**, 41−63 (1997).

25 Bilger, R.W., Starner, S.H., Kee, R.J., "On reduced mechanisms for methane-air combustion in nonpremixed flames", *Combust. Flame*, **80**, 135−149 (1990).

26 Bombach, R., Käppeli, B., "Simultaneous visualisation of transient species in flames by planar-laser-induced fluorescence using a single laser system", *Appl. Phys. B.*, **68** (2), 251−255 (1999).

27 Medwel, P.R., "Laser diagnostics in MILD combustion", Ph.D. Thesis, University of Adelaide, Australia (2007).

28 Gardiner, J.W.C., Combustion Chemistry, Springer-Verlag, New York (1984).